

RDFC-GAN: RGB-Depth Fusion CycleGAN for Indoor Depth Completion

Haowen Wang*, Zhengping Che*, *Member, IEEE*, Mingyuan Wang, Zhiyuan Xu, *Member, IEEE*,
Xiuquan Qiao[✉], Mengshi Qi, Feifei Feng, and Jian Tang[✉], *Fellow, IEEE*

Abstract—The raw depth image captured by indoor depth sensors usually has an extensive range of missing depth values due to inherent limitations such as the inability to perceive transparent objects and the limited distance range. The incomplete depth map with missing values burdens many downstream vision tasks, and a rising number of depth completion methods have been proposed to alleviate this issue. While most existing methods can generate accurate dense depth maps from sparse and uniformly sampled depth maps, they are not suitable for complementing large contiguous regions of missing depth values, which is common and critical in images captured in indoor environments. To overcome these challenges, we design a novel two-branch end-to-end fusion network named RDFC-GAN, which takes a pair of RGB and incomplete depth images as input to predict a dense and completed depth map. The first branch employs an encoder-decoder structure, by adhering to the Manhattan world assumption and utilizing normal maps from RGB-D information as guidance, to regress the local dense depth values from the raw depth map. In the other branch, we propose an RGB-depth fusion CycleGAN to transfer the RGB image to the fine-grained textured depth map. We adopt adaptive fusion modules named W-AdaIN to propagate the features across the two branches, and we append a confidence fusion head to fuse the two outputs of the branches for the final depth map. Extensive experiments on NYU-Depth V2 and SUN RGB-D demonstrate that our proposed method clearly improves the depth completion performance, especially in a more realistic setting of indoor environments, with the help of our proposed pseudo depth maps in training.

Index Terms—Depth completion, Generative adversarial network, RGB-depth fusion, Indoor environment

I. INTRODUCTION

DEPTH sensors have been widely used to provide reliable 3D spatial information in a variety of applications, such as augmented reality, indoor navigation, and 3D reconstruction tasks [3]–[5]. However, most existing commercial depth sensors (*e.g.*, Kinect [6], RealSense [7], and Xtion [8]) for indoor spatial perception are not powerful enough to generate a precise and lossless depth map, as shown in the top row of Fig. 1. These sensors often produce many hole regions

H. Wang, M. Wang, and X. Qiao are with State Key Laboratory of Networking and Switching Technology, Beijing University of Posts and Telecommunications, China. E-mail: {hw.wang, wmingyuan, qiaoxq}@bupt.edu.cn

Z. Che, Z. Xu, F. Feng, and J. Tang are with Midea Group, China. E-mail: chezhengping@gmail.com and {chezp, xuzhy70, feifei.feng, tangjian22}@midea.com

M. Qi is with School of Computer Science, Beijing University of Posts and Telecommunications, China. E-mail: qms@bupt.edu.cn

This work was done during H. Wang’s internship at Midea Group. A preliminary version [1] of this paper was presented at the 35th IEEE/CVF Conference on Computer Vision and Pattern Recognition (CVPR), 2022.

*The first two authors (H. Wang and Z. Che) contributed equally.

✉Corresponding Authors: X. Qiao and J. Tang.

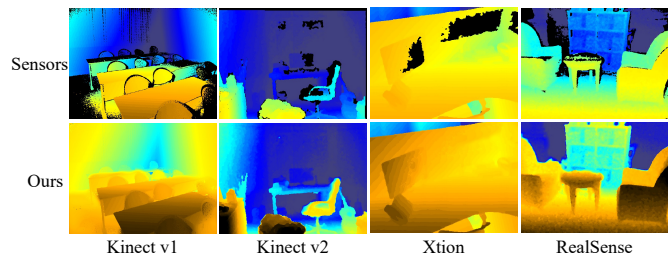


Fig. 1. Showcases of the raw depth maps (top) in indoor scenarios collected by different sensors from the SUN RGB-D dataset [2] and the corresponding depth completion results (bottom) of our method.

with invalid depth pixels due to transparent, shining, and dark surfaces as well as too close or too far edges, and these holes significantly affect the performance of downstream tasks on the depth maps (a.k.a., depth images). To address the issue from imperfect depth maps, there have been a lot of approaches to reconstruct the whole depth map from the raw depth map, called *depth completion*. As RGB images provide rich color and texture information compared with depth maps, the aligned RGB image is commonly used to guide the depth completion of a depth map. To be more specific, the depth completion task is usually conducted as using a pair of raw depth and RGB images captured by one depth sensor to complete and refine the depth values.

Recent studies have produced significant progress in depth completion tasks with convolutional neural networks (CNNs) [9]–[14]. Ma and Karaman [10] introduced an encoder-decoder network to directly regress the dense depth map from a sparse depth map and an RGB image. The method has shown great progress compared to conventional algorithms [15]–[17], but its predicted dense depth maps are often too blurry due to inadequate capturing of local information. To generate a more refined completed depth map, lots of works have recently arisen, which can be divided into two groups with different optimization methods. The first group of works [9], [14], [18] learn affinities for relative pixels and iteratively refine depth predictions, which highly rely on the accuracy of the raw global depth map and suffer the inference inefficiency. Other works [11]–[13], [19] analyze the geometric characteristic and adjust the feature network structure accordingly, for instance, by estimating the surface normal or projecting depth into discrete planes. In any case, these methods merely use the RGB image as superficial guidance or auxiliary information and require approximate

depth completeness without missing regions. Also, the model parameters may not be efficiently generalized to different scenes, as few methods deeply consider the textural and contextual information, and the model parameters may not be efficiently generalized to different scenes. At this point, the depth completion task is more or less degraded to a monocular depth estimation task that is conceptually simple but practically difficult.

It is also worth noting that depth completion in indoor environments, due to its special properties, has not been well-addressed by existing depth completion methods. Prevailing depth completion approaches [11]–[13], [19], [20] emphasize intricate adaptive propagation structures for local pixels, which may fail in dealing with large invalid depth maps that are prevalent in indoor scenes. Furthermore, it is common that man-made houses follow regular geometric structures, such as mutual perpendicular-oriented walls, floors, and ceilings. This domain knowledge, usually referred to as Manhattan world assumption [21], can help people easily tell invalid and unreasonable depth estimation results and has been properly used in SLAM [22], monocular depth estimation [23], and 3D reconstruction [24]. However, to effectively incorporate this structural regularity in depth completion methods, especially with the fusion of RGB and depth images, is unexplored.

More remarkably, most existing methods [9], [10], [19] only consider completing sparse depth images and uniformly randomly sample a certain number of valid pixels from the raw or complete dense depth image as the input for training and evaluation. While such downsampling setting mimics well the task of outdoor depth completion from *raw Lidar scans* to dense annotations (as shown in the bottom row of Fig. 2), it is improper for indoor RGB-depth sensor data, since the sampled patterns are quite different from the real missing patterns in indoor scenes, such as large missing regions and semantical missing patterns. Specifically, as shown in the top row of Fig. 2, the raw depth map captured by indoor depth sensors is dense and continuous, which is quite different from the sparse pattern of downsampled input. Meanwhile, the downsampled input leaks the ground truth depth values in the mimicked missing regions to the completion models, leading to flawed evaluations. Therefore, though existing methods are shown to be effective for completing uniformly sparse depth maps, it remains unverified whether they perform well enough for indoor depth completion in practice. This should be addressed by reasonable training strategies and comprehensive evaluation settings specifically designed for indoor scenarios.

To solve these problems in indoor depth completion, we propose a novel two-branch end-to-end network to generate a completed dense depth map for indoor environments. On one hand, inspired by a series of generative adversarial networks (GANs) [25]–[28] including CycleGANs [29], [30] that can effectively capture and exploit texture style information, we propose an *RGB-depth Fusion CycleGAN* (RDFC-GAN) branch for fusing an RGB image and a depth map. RDFC-GAN maps an RGB image from the RGB domain to a complete depth map in the depth domain through the latent spatial vector generated by the incomplete depth map. On the other hand, we design a *Manhattan-Constraint*

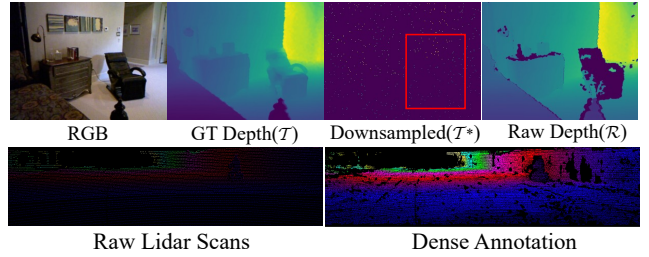


Fig. 2. Depth data visualizations of indoor RGB-Depth sensor data (top, NYU-Depth V2) and outdoor Lidar scan data (bottom, KITTI). The downsampled data (T^*) is 500 pixels randomly and uniformly sampled from the ground-truth (GT) depth data (T), which contains ground truth depth values (e.g., in the red box) that do not exist in the raw depth data (R).

Network (MCN) branch that leverages the Manhattan world assumption in a generated normal map to guide the depth completion in indoor scenes. In order to connect these two branches and restrict the estimated depth, we introduce *weighted adaptive instance normalization* (W-AdaIN) modules. Afterwards, a *confidence fusion head* concludes the final depth map completion.

In addition, we propose to produce pseudo depth maps for training by sampling raw depth images. According to the characteristic of the indoor depth missing, we utilize the RGB images and semantic labels to produce masking regions for raw depth maps, which is more realistic than the simple uniform sampling. Experiments show that the model learning from pseudo depth maps can more effectively fill in large missing regions for raw depth images captured indoors.

Our main contributions are summarized as the following:

- We propose a novel end-to-end network named RDFC-GAN that effectively fuses a raw depth map and an RGB image to reproduce a reasonable and complete dense depth map.
- We design the Manhattan-constraint network utilizing the geometry properties of indoor scenes, which effectively introduce smoother depth value constraints and further boosts the performance of RDFC-GAN.
- We design and utilize the pseudo depth maps, which are in line with the raw depth missing distribution in indoor scenarios. Training with pseudo depth maps significantly improves the model’s depth completion performance, especially in more realistic settings of indoor environments.
- We show that our proposed method achieves the state-of-the-art performance on NYU-Depth V2 and SUN RGB-D for depth completion with comprehensive evaluation metrics and prove its effectiveness in improving downstream task performance such as object detection.

II. RELATED WORK

1) *Depth Completion*: Recent works have extensively applied deep neural networks for depth completion tasks with remarkable improvements. Ma and Karaman [10] used a CNN encoder-decoder to predict the full-resolution depth image from a set of depth samples and RGB images. On this basis, several methods [11], [12], [19], [31], [32] incorporating additional representations or auxiliary outputs have been proposed. Qiu *et al.* [11] produced dense depth using the surface

normal as the intermediate representation. Huang *et al.* [12] applied the boundary consistency to solve the issue of vague structures. Imran *et al.* [33] introduced the depth coefficients to address the challenge of depth smearing between objects. Lee *et al.* [19] introduced the Plane-Residual representation to interpret depth information and factorized the depth regression problem into a combination of discrete depth plane classification and plane-by-plane residual regression. Chen *et al.* [34] converted the depth map to the point clouds and take advantages of a geometry-aware embedding to fill in missing depth information. Another series of methods [9], [14], [20] have introduced new network structures to depth completion tasks. Cheng *et al.* [9] proposed the convolutional spatial propagation network (CSPN) and generated the long-range context through a recurrent operation. Gansbeke *et al.* [35] used a fusion structure and confidence masks to account for depth completion uncertainty from each modality. Li *et al.* [36] introduced a multi-scale guided cascade hourglass network to capture structures at different levels. Senushkin *et al.* [37] controlled the depth decoding for different regions via spatially-adaptive denormalization blocks. NLSPN [14] improved CSPN by non-local spatial and global propagations. DySPN [20] and GraphCSPN [38] further enhance the performance of sparse depth completion tasks. In this work, to build our depth completion model, we both include new representations and extend the network structure.

2) *RGB-D Fusion*: The fusion of both RGB and depth data (a.k.a., the RGB-D fusion) is essential in many tasks such as semantic segmentation [39]–[41], scene reconstruction [42]–[44], and navigation [45]–[47]. While early works [10], [48] only concatenate aligned pixels from RGB and depth features, more effective RGB-D fusion methods have been proposed recently. Cheng *et al.* [49] designed a gated fusion layer to learn different weights of each modality in different scenes. Park *et al.* [50] fused multi-level RGB-D features in a

very deep network through residual learning. Du *et al.* [51] proposed a cross-modal translate network to represent the complementary information and enhance the discrimination of extracted features. In this work, we design the two-branch structure and progressively deploy the W-AdaIN modules to better capture and fuse RGB and depth features.

3) *Generative Adversarial Networks*: Generative adversarial networks (GANs) [25] have achieved great success in a variety of image generation tasks such as style transfer [52]–[54], realistic image generation [55], [56], and image synthesis [57], [58]. Mirza *et al.* [25] proposed the conditional GAN to direct the data generation process by combining the additional information as a condition. CycleGAN [59] maintains the inherent features of the source domain while translating to the target domain through the cycle consistency. Karras *et al.* [27] introduced a style-based GAN to embed the latent code into a latent space to affect the variations of generated images. In this work, we use a GAN-based structure to generate dense depth maps with fine-grained textures.

4) *Indoor Structural Regularities*: The Manhattan world assumption [21] takes advantage of the prevalent orthogonal directions in human-made environments, thereby streamlining tasks by diminishing the intricacy of the associated structures. An increasing number of methods [24], [60], [61] leverage it for indoor vision tasks. For example, in 3D room layout estimation tasks, some works [60]–[64] simplify task complexity by transforming corner points or junctions into intersecting vertical planes. Li *et al.* [23] exploited the inherent structural regularities to improve monocular depth estimation. In 3D scene understanding and reconstruction, Manhattan world assumption has been integrated as connections between 3D scenes and 2D images [65] or as additional constraints [24], [66], [67]. In this work, we introduce the Manhattan world assumption into depth completion tasks for the first time.

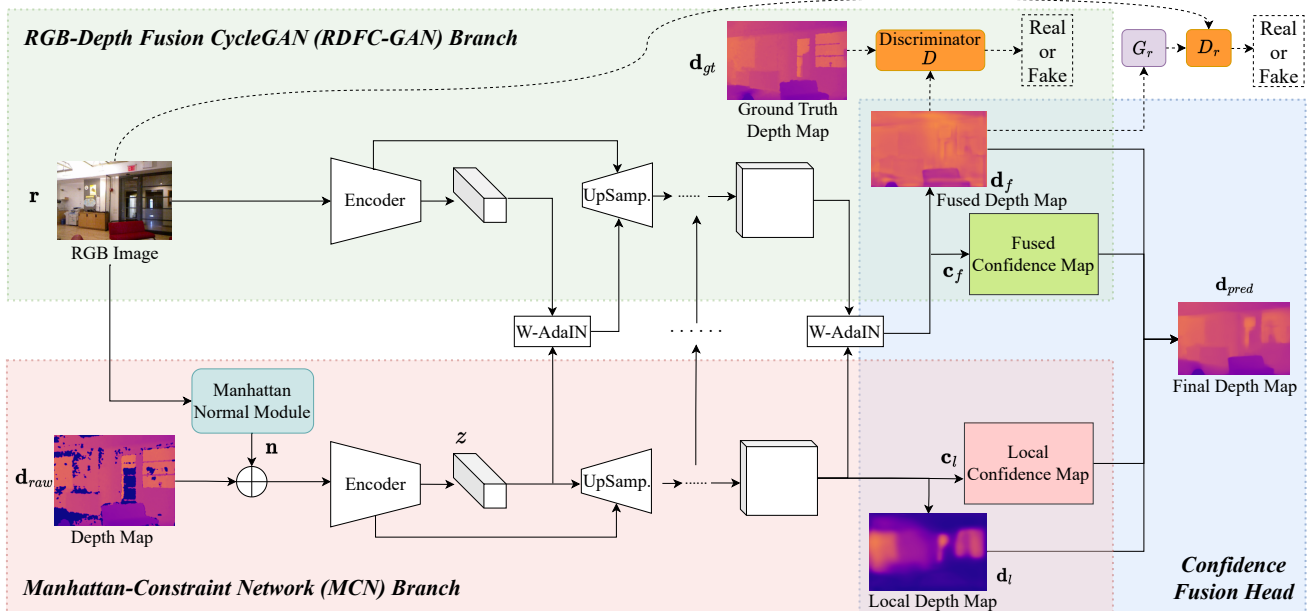


Fig. 3. The overview of the proposed end-to-end depth completion method (RDFC-GAN).

III. METHOD

In this section, we describe our end-to-end depth completion method, as shown in Fig. 3. The proposed model takes a raw (noisy and possibly incomplete) depth map $\mathbf{d}_{\text{raw}} \in \mathbb{R}^{H \times W \times 1}$ and its corresponding RGB image $\mathbf{r} \in \mathbb{R}^{H \times W \times 3}$ as the input, and outputs the completed and refined dense depth map estimation (a.k.a, final depth map) $\mathbf{d}_{\text{pred}} \in \mathbb{R}^{H \times W \times 1}$ to be close to the ground truth depth map $\mathbf{d}_{\text{gt}} \in \mathbb{R}^{H \times W \times 1}$, where H and W are the height and the width of the depth map, respectively.

The model mainly consists of two branches: a Manhattan-Constraint Network (MCN) branch (Section III-A) and an RGB-depth Fusion CycleGAN (RDFC-GAN) branch (Section III-B). MCN and RDFC-GAN take the depth map and the RGB image as the input, respectively, and produce their individual depth completion results. To fuse the representations between the two branches, a series of intermediate fusion modules called W-AdaIN (Section III-C) are deployed at different stages of the model. Finally, a confidence fusion head (Section III-D) combines the outputs of the two channels and provides more reliable and robust depth completion results. Moreover, we introduce the training strategy with pseudo depth maps (Section III-E) and describe the overall loss function for training (Section III-F).

A. The Manhattan-Constraint Network (MCN) Branch

The first branch, Manhattan-Constraint Network (MCN) branch, is composed of a Manhattan normal module and a convolutional encoder-decoder structure. As illustrated in the bottom-left part of Fig. 3, this branch mainly relies on the raw depth map, as well as auxiliary from the RGB image, and outputs a dense local depth map $\mathbf{d}_l \in \mathbb{R}^{H \times W \times 1}$ and a local confidence map $\mathbf{c}_l \in \mathbb{R}^{H \times W \times 1}$.

1) *Manhattan Normal Module*: Depth prediction in coplanar regions can benefit from known surface normals [68], [69]. However, estimating surface normals in indoor scenes is challenging due to pervasive large untextured planes with consistent luminosity in rooms. To address this, we design a Manhattan normal module to leverage the Manhattan World assumption [21] that most surfaces in indoor scenes are usually orthogonal and aligned with three dominant directions, which is shown in Fig. 4. On one hand, we employ a pretrained segmentation network [70] to identify floor, ceiling, and wall regions in the RGB scene. Also, we use a U-Net [71] as

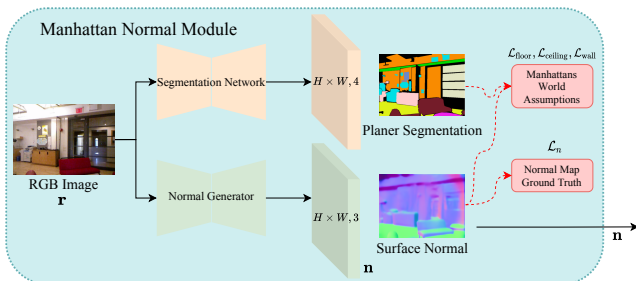


Fig. 4. An Illustration of the Manhattan normal module in the Manhattan-Constraint network (MCN).

a normal generator to generate a normal map that can both approximate the ground-truth and follow the Manhattan assumption.

Specifically, for all predicted normal vectors $\mathbf{n}_p \in \mathbb{R}^3$ where p refers to any pixel, we optimize the cosine similarity loss \mathcal{L}_n between the predicted normal vectors and the ground-truth normal map by

$$\mathcal{L}_n = -\frac{1}{HW} \sum_p \frac{\mathbf{n}_p \cdot \mathbf{n}_p^*}{\|\mathbf{n}_p\| \cdot \|\mathbf{n}_p^*\|}, \quad (1)$$

where \mathbf{n}^* is the ground-truth. For planar regions, we incorporate the information from segmentation results (i.e., whether each pixel p belongs to the floor, ceiling, wall, or none) and ensure the normals to be consistent with plane physical orientations. For example, we enforce all floor points to be upward perpendicular oriented by

$$\mathcal{L}_{\text{floor}} = -\frac{1}{\sum_p \mathcal{I}(p \in \text{floor})} \sum_p \frac{\mathbf{n}_p \cdot \mathbf{v}_z}{\|\mathbf{n}_p\|} \mathcal{I}(p \in \text{floor}), \quad (2)$$

where $\mathbf{v}_z = (0, 0, 1)$ is the upward perpendicular unit normal vector, and $\mathcal{I}(\cdot)$ is the indicator function. Similarly, for ceiling and wall, we have

$$\mathcal{L}_{\text{ceiling}} = \frac{1}{\sum_p \mathcal{I}(p \in \text{ceiling})} \sum_p \frac{\mathbf{n}_p \cdot \mathbf{v}_z}{\|\mathbf{n}_p\|} \mathcal{I}(p \in \text{ceiling}), \quad (3)$$

$$\mathcal{L}_{\text{wall}} = \frac{1}{\sum_p \mathcal{I}(p \in \text{wall})} \sum_p \frac{|\mathbf{n}_p \cdot \mathbf{v}_z|}{\|\mathbf{n}_p\|} \mathcal{I}(p \in \text{wall}). \quad (4)$$

In summary, the loss for Manhattan normal module is

$$\mathcal{L}_{\text{MNM}} = \mathcal{L}_n + \mathcal{L}_{\text{floor}} + \mathcal{L}_{\text{ceiling}} + \mathcal{L}_{\text{wall}}. \quad (5)$$

2) *Encoder-Decoder Structure*: The output of the Manhattan normal module (i.e., a three-channel map $\mathbf{n} \in \mathbb{R}^{H \times W \times 3}$) is concatenated with the one-channel raw depth image \mathbf{d}_{raw} to form the input to an encoder-decoder. The encoder-decoder of MCN, as shown in Fig. 5, is based on ResNet-18 [72] and pre-trained on the ImageNet dataset [73]. Given this input, the encoding stage downsamples the feature size by 32 times and expands the feature dimension to 512. The encoder learns the mapping from the depth map space to the depth latent space and produce $\mathbf{z} \in \mathbb{R}^{\frac{H}{32} \times \frac{W}{32} \times 512}$ as the fused depth feature

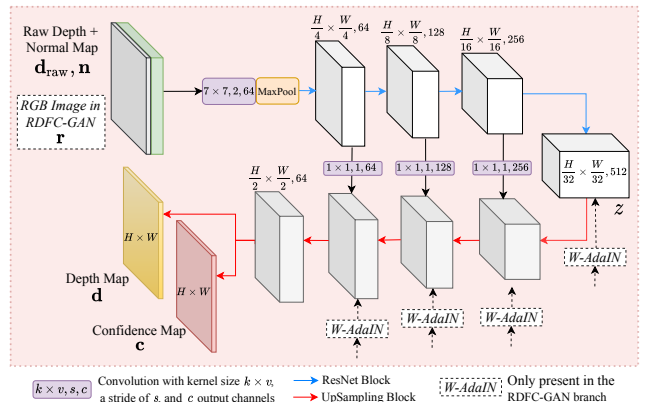


Fig. 5. An Illustration of the encoder-decoder structure in the two branches.

information. The decoding stage applies a set of upsampling blocks to increase the feature resolution with skip connection from the encoder. The output of the decoder is a local depth map and its corresponding local confidence map, which is the final output of the MCN branch.

The overall loss for the MCN branch \mathcal{L}_{MCN} also includes the L_1 loss on the local depth map, i.e.,

$$\mathcal{L}_{\text{MCN}} = \mathcal{L}_{\text{MNM}} + \lambda_1 \|\mathbf{d}_l - \mathbf{d}_{\text{gt}}\|_1, \quad (6)$$

where λ_1 is the weight hyperparameter for the L_1 loss.

B. The RGB-Depth Fusion CycleGAN (RDFC-GAN) Branch

To generate the fine-grained textured and dense depth map, we propose the second branch in our model, which is a GAN-based structure for RGB and depth image fusion, as illustrated in the top-left part of Fig. 3. Different from most existing fusion methods that directly concatenate inputs from different domains, our fusion model, inspired by the conditional and style GANs [25], [27], a) uses the depth latent vector mapping from incomplete depth image as the input and the RGB image as the condition to generate a dense fused depth prediction $\mathbf{d}_f \in \mathbb{R}^{H \times W \times 1}$ and a fused confidence map $\mathbf{c}_f \in \mathbb{R}^{H \times W \times 1}$, and b) uses a discriminator to distinguish the ground truth depth images from generated ones.

The generator $G(\cdot)$ has a similar structure as the encoder-decoder of MCN shown in Fig. 5, except for the RGB-only input and the fusion with W-AdaIN. Given the corresponding RGB image \mathbf{r} as the condition, the generator $G(\cdot)$ with the depth latent vector \mathbf{z} generates a fused dense depth map \mathbf{d}_f and a fused confidence map \mathbf{c}_f for the scene. The latent vector \mathbf{z} from MCN propagates the depth information to the RGB image using the proposed W-AdaIN described later in Section III-C. We distinguish the fused depth map \mathbf{d}_f and the real depth image \mathbf{d}_{gt} by the discriminator $D(\cdot)$, whose structure is based on PatchGAN [29].

Besides the main GAN structure, to enhance the effects of texture information in generating depth maps, we form a structure of CycleGAN [59] with an auxiliary pair of generator $G_r(\cdot)$ and discriminator $D_r(\cdot)$, which generate RGB images from depth maps and distinguishing generated RGB images from real RGB images, respectively. $G_r(\cdot)$ employs the ResNet-18 architecture [72], and $D_r(\cdot)$ follows the same architecture as $D(\cdot)$ except no condition inputs.

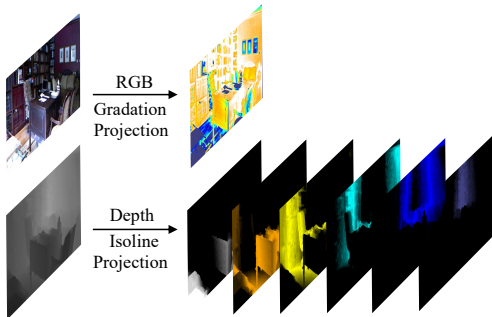


Fig. 6. Examples of projecting an RGB image to color gradations (top) and projecting a depth map to different depth planes (bottom).

We adopt the objective functions of WGAN [74] and CycleGAN [59] for training RDFC-GAN. To be more specific, the RDFC-GAN loss includes two discriminator losses (\mathcal{L}_D and \mathcal{L}_{D_r}), two generator losses (\mathcal{L}_G and \mathcal{L}_{G_r}), and a cycle loss ($\mathcal{L}_{\text{cycle}}$) as

$$\mathcal{L}_D = D(G(\mathbf{d}_{\text{raw}}, \mathbf{r}) | \mathbf{r}) - D(\mathbf{d}_{\text{gt}} | \mathbf{r}), \quad (7)$$

$$\mathcal{L}_G = -D(G(\mathbf{d}_{\text{raw}}, \mathbf{r}) | \mathbf{r}), \quad (8)$$

$$\mathcal{L}_{D_r} = D_r(G_r(\mathbf{d}_{\text{gt}})) - D_r(\mathbf{r}), \quad (9)$$

$$\mathcal{L}_{G_r} = -D_r(G_r(\mathbf{d}_{\text{gt}})), \quad (10)$$

$$\mathcal{L}_{\text{cycle}} = \|G_r(G(\mathbf{d}_{\text{raw}}, \mathbf{r})) - \mathbf{r}\|_1 + \|G(G_r(\mathbf{d}_{\text{gt}})) - \mathbf{d}_{\text{gt}}\|_1, \quad (11)$$

where the discriminator and generator losses only affect the corresponding discriminator and generator, respectively.

The overall loss for the RDFC-GAN branch $\mathcal{L}_{\text{RDFC}}$ combines all the loss terms above, i.e.,

$$\mathcal{L}_{\text{RDFC}} = \mathcal{L}_D + \mathcal{L}_G + \mathcal{L}_{D_r} + \mathcal{L}_{G_r} + \mathcal{L}_{\text{cycle}}. \quad (12)$$

C. W-AdaIN: Weighted Adaptive Instance Normalization

To allow the feature information to be shared across all stages of the two branches, we design and apply the W-AdaIN module in the network. As illustrated in Fig. 6, we project depth pixels from the depth map onto multiple discretized depth planes, based on the distance between depth pixels and a predetermined set of discrete depth values. Due to similar depth values, local regions are easier to be classified into the same depth plane. We also find that similar color gradations within local regions generally have similar depth values. To utilize these observations, we propose a Weighted Adaptive Instance Normalization (W-AdaIN) module for effectively fusing the features of RGB and depth images. It is built upon AdaIN [27] and is defined as

$$\text{W-AdaIN}(\mathbf{z}, \mathbf{f}_r) = \text{Attn}(\mathbf{z}) \cdot y_s \cdot \frac{\mathbf{f}_r - \mu(\mathbf{f}_r)}{\sigma(\mathbf{f}_r)} + \text{Attn}(\mathbf{f}_r) \cdot y_b, \quad (13)$$

where \mathbf{z} is the depth feature map from MCN's intermediate stage, \mathbf{f}_r is the RGB image feature map from RDFC-GAN's corresponding stage, $\text{Attn}(\cdot)$ is the self-attention module [75], y_s and y_b are the spatial scaling and bias factors obtained by affine transformations on \mathbf{z} , and $\mu(\cdot)$ and $\sigma(\cdot)$ are the mean and variance, respectively. The design of W-AdaIN enables $\text{Attn}(\mathbf{z})$ to assign similar weight values to regions with similar depth values and $\text{Attn}(\mathbf{f}_r)$ to smooth depth blocks with locally similar color gradations by similar weight values. This fusion strategy is applied after each upsampling block in both decoders, improving depth estimation and scene understanding by leveraging the complementary information present in both RGB and depth images.

D. Confidence Fusion Head

In our framework, either branch has its role. The MCN branch, with an encoder-decoder structure, generates a locally accurate depth map by relying more on valid raw depth

information. The RDFC-GAN branch estimates the missing depth based on the textural features of the RGB image but may produce obvious outliers, i.e., estimation deviations from the raw depth values. Hence, we introduce the confidence maps [35] to integrate the depth maps from two branches by a confidence fusion head, which is shown in the right of Fig. 3. The confidence maps assign more attention to reliable depth prediction regions through the learned confidence. In general, the local depth map obtains higher confidences in regions whose raw depth values are more accurate, while the fused depth map has higher confidences in large missing and noisy regions. The sum of the two depth maps weighted by the corresponding confidence maps is the final depth prediction \mathbf{d}_{pred} , which is formulated as

$$\mathbf{d}_{\text{pred}}(i, j) = \frac{e^{c_l(i, j)} \mathbf{d}_l(i, j) + e^{c_r(i, j)} \mathbf{d}_r(i, j)}{e^{c_l(i, j)} + e^{c_r(i, j)}}, \quad (14)$$

where $1 \leq i \leq H$, $1 \leq j \leq W$, and $\mathbf{x}(i, j)$ refers to the (i, j) -th value of variable \mathbf{x} .

E. Pseudo Depth Map for Training

Most existing depth completion methods are trained and evaluated with the random sparse sampling method [10], [14], [19]. The sampled depth map mimics outdoor depth well, but its depth distribution and missing patterns are quite different from the real indoor depth completion scene, as compared in Fig. 2. For example, the randomly downsampled depth pixels cover almost all areas of the scene, while the missing depth pixels in indoor environments usually form continuous areas.

Hence, we propose a set of synthetic methods to produce depth maps for indoor depth completion model training, which rely on RGB images and semantic masks to map the raw depth image to reasonable incomplete (pseudo) depth maps. Pseudo depth map mimics the depth missing patterns and is more like real raw depth data in indoor environments than the randomly sampled depth maps. We design five methods to obtain the pseudo depth map:

- (1) *Highlight masking*. RGB-D cameras have difficulty in obtaining depth data of shiny surfaces because IR rays reflected from shiny surfaces are weak or scattered [76], and smooth and shiny objects often lead to specular highlights and bright spots in the RGB images. Hence,

we detect highlight regions in RGB images [77] and mask them in depth maps to generate pseudo depth maps.

- (2) *Black masking*. Dark and matte surfaces absorb rather than reflecting radiations which strongly affected the depth map values [78]. We randomly mask the depth pixels whose RGB values are all in $[0, 5]$ to directly mimic invalid depth values in dark regions.
- (3) *Graph-based segmentation masking*. Chaotic light reflections in the complex environment interfere with the return of infrared light and cause discrete and irregular noises in depth maps. To simulate this phenomenon, we use the graph-based segmentation [79] to divide the RGB image into blocks and randomly mask some small blocks.
- (4) *Semantic masking*. Some materials, such as glass, mirror, and porcelain surfaces, easily cause scattered infrared reflection and missing depth values. We utilize the semantic label information to locate objects probably containing these materials, such as televisions, mirrors, and windows, and we randomly mask one or two such objects (but keep depth pixels on their edges) in each frame.
- (5) *Semantic XOR masking*. With the similar motivation to (3) the graph-based segmentation masking, we use semantic segmentation to recognize complex regions and mask depth values in these regions. The complex region is defined as those whose predicted segmentation results, segmented by a U-Net [80] trained on 20% RGB images of the training set, are different from the ground-truth. In other words, we conduct the Exclusive Or (XOR) operation on the segmentation results and the ground-truth to obtain the masking.

Finally, we randomly pick and combine the mask from the above five methods to generate the pseudo depth map from the raw depth, mimicking a more plausible missing depth distribution. The pseudo depth maps are used to train a more robust depth completion model for indoor scenarios.

F. Overall Loss Function

We train all the network in an end-to-end way, with all previously described losses and the L_1 loss on the final prediction. The overall loss function is defined as:

$$\mathcal{L}_{\text{overall}} = \mathcal{L}_{\text{MCN}} + \mathcal{L}_{\text{RDFC}} + \lambda_{\text{pred}} \|\mathbf{d}_{\text{pred}} - \mathbf{d}_{\text{gt}}\|_1, \quad (15)$$

where λ_{pred} is the weight hyperparameter for the L_1 loss.

IV. EXPERIMENTS

A. Datasets

We conducted experiments on two widely-used benchmarks: NYU-Depth V2 [81] and SUN RGB-D [2].

1) *NYU-Depth V2*: The NYU-Depth V2 dataset [81] contains pairs of RGB and depth images collected from Microsoft Kinect in 464 indoor scenes. The dataset comprises densely labeled data samples divided into the training set with 795 images and the test set with 654 images. Each sample includes an RGB image, a raw depth image captured by sensors, a reconstructed depth map treated as ground-truth labels, and a segmentation mask. The dataset also has about 50,000

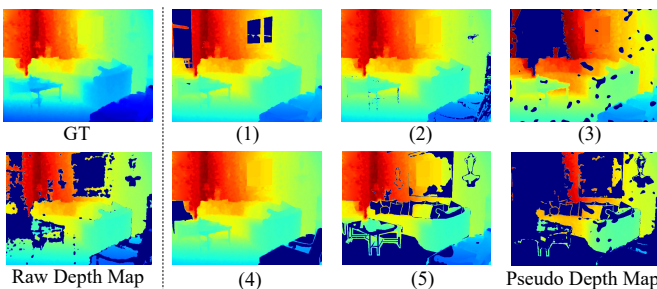


Fig. 7. Visualizations of the proposed pseudo depth map and five sampling methods. ‘GT’ refers to the reconstructed (ground-truth) depth map. The shown pseudo depth map is generated from the raw depth map by applying all five sampling methods together.

unlabeled data samples with only RGB and raw images. Following existing methods [10], [14], we trained on the unlabeled images and the training set, and we used the test set for evaluation. All images were resized to 320×240 and center-cropped to 304×228 .

2) *SUN RGB-D*: The SUN RGB-D dataset [2] contains 10,335 RGB-D images captured by four different sensors, offering a diverse and comprehensive collection of scenes that effectively facilitate the evaluation of model generalization. Moreover, the dataset has dense semantic segmentation and 3D bounding box annotations that enables downstream task (e.g., object detection) evaluations. Following the official dataset split [2], we used 4,845 images for training and 4,659 for testing and used the refined depth map derived from multiple frames [2] as the ground truths for evaluation. All images were resized to 320×240 and randomly cropped to 304×228 .

B. Evaluation Metrics

To comprehensively assess the performance of depth completion methods, we employed common metrics in both the original depth space and the point cloud space, as well as depth map and point cloud visualizations for qualitative evaluation.

1) *Depth Values*: We adopted three metrics that measures on the depth values directly: the root mean squared error (RMSE), the absolute relative error (Rel), and δ_{th} as proposed by Ma *et al.* [10].

RMSE is sensitive to substantial errors and offers valuable insight of the overall accuracy, which is defined as

$$\text{RMSE} = \sqrt{\frac{1}{HW} \sum_{i,j} (\mathbf{d}_{\text{pred}}(i,j) - \mathbf{d}_{\text{gt}}(i,j))^2}. \quad (16)$$

Rel assesses the relative error by normalizing the absolute deviation by the ground truth. Rel is defined as

$$\text{Rel} = \frac{1}{HW} \sum_{i,j} \frac{|\mathbf{d}_{\text{pred}}(i,j) - \mathbf{d}_{\text{gt}}(i,j)|}{\mathbf{d}_{\text{gt}}(i,j)}. \quad (17)$$

δ_{th} measures the percentage of predicted pixels whose relative error is within the relative threshold th . The mathematical expression for δ_{th} is

$$\delta_{th} = \frac{1}{HW} \sum_{i,j} \mathcal{I} \left(\max \left(\frac{\mathbf{d}_{\text{pred}}(i,j)}{\mathbf{d}_{\text{gt}}(i,j)}, \frac{\mathbf{d}_{\text{gt}}(i,j)}{\mathbf{d}_{\text{pred}}(i,j)} \right) < th \right), \quad (18)$$

where $\mathcal{I}(\cdot)$ is the indicator function. With the same threshold value, a higher δ_{th} value indicates better consistency of the depth completion results.

2) *Point Clouds*: We noticed that the metrics on depth values effectively assess the global accuracy but inadequately address local outliers. Consequently, we proposed to transform completed depth maps into point clouds and measured the Chamfer distance (CD) and the averaged F1 score (F_1) for a thorough evaluation. Both CD and F_1 adeptly capture the geometric structure and relative positional relationships between point clouds, thereby exhibiting heightened sensitivity to local anomalies and noise.

To convert depth maps (\mathbf{d}_{pred} and \mathbf{d}_{gt}) into point clouds ($\mathcal{P}_{\text{pred}}$ and \mathcal{P}_{gt}), we employed the following formula

for each pixel (i, j) in the depth map to get the corresponding point $\mathbf{p} = (x, y, z)$ in the point cloud:

$$[x, y, z]^\top = \mathbf{d}(i, j) \mathbf{K}^{-1}[i, j, 1]^\top, \quad (19)$$

where \mathbf{K} represents the intrinsic matrix of the camera.

The Chamfer distance (CD) is a symmetric distance metric between two point clouds, defined as

$$\text{CD} = \frac{1}{|\mathcal{P}_{\text{gt}}|} \sum_{\mathbf{p} \in \mathcal{P}_{\text{gt}}} \min_{\mathbf{p}' \in \mathcal{P}_{\text{pred}}} \|\mathbf{p} - \mathbf{p}'\|^2 + \frac{1}{|\mathcal{P}_{\text{pred}}|} \sum_{\mathbf{p}' \in \mathcal{P}_{\text{pred}}} \min_{\mathbf{p} \in \mathcal{P}_{\text{gt}}} \|\mathbf{p} - \mathbf{p}'\|^2, \quad (20)$$

where $|\mathcal{P}_{\text{gt}}|$ and $|\mathcal{P}_{\text{pred}}|$ denotes the number of points in \mathcal{P}_{gt} and $\mathcal{P}_{\text{pred}}$, respectively, \mathbf{p} and \mathbf{p}' denote points in the 3D space, and $\|\cdot\|$ is the Euclidean distance.

The averaged F1 score (F_1) is defined as the average of the harmonic mean of precision (Prec_Δ) and recall (Rec_Δ) with a distance threshold Δ (Unit: meter):

$$\text{Prec}_\Delta = \frac{1}{|\mathcal{P}_{\text{pred}}|} \sum_{\mathbf{p} \in \mathcal{P}_{\text{pred}}} \mathcal{I} \left(\min_{\mathbf{p}' \in \mathcal{P}_{\text{gt}}} \|\mathbf{p} - \mathbf{p}'\| < \Delta \right), \quad (21)$$

$$\text{Rec}_\Delta = \frac{1}{|\mathcal{P}_{\text{gt}}|} \sum_{\mathbf{p} \in \mathcal{P}_{\text{gt}}} \mathcal{I} \left(\min_{\mathbf{p}' \in \mathcal{P}_{\text{pred}}} \|\mathbf{p} - \mathbf{p}'\| < \Delta \right), \quad (22)$$

$$F_1 = \frac{1}{3} \sum_{\Delta \in \{0.02, 0.03, 0.04\}} \frac{2}{\text{Prec}_\Delta^{-1} + \text{Rec}_\Delta^{-1}}, \quad (23)$$

where $\mathcal{I}(\cdot)$ is the indicator function and Δ determines whether two points are matched (i.e., closely enough).

C. Implementation Details

For the MCN branch, the segmentation results were from a pre-trained and frozen PSPNet [70] with a ResNet-50 backbone, and the normal map generator was a pre-trained U-Net [71] that was jointly trained with other modules. The RDFC-GAN branch and other parts of the proposed network were trained from scratch. The weights and bias in $G(\cdot)$, $G_r(\cdot)$, $D(\cdot)$, and $D_r(\cdot)$ were initialized from $\mathcal{N}(0, 0.02^2)$ and 0, respectively. The values of λ_1 and λ_{pred} were set to 0.5 and 5, respectively. The optimizer for MCN was AdamW [82] with a weight decay of 0.01 and an initial learning rate lr_0 of 0.002. The optimizers for other modules were Adam [83] with an initial learning rate lr_0 of 0.004. All optimizers had $\beta_1 = 0.5$, $\beta_2 = 0.999$. We trained the network 150 epochs and used a linear learning rate scheduler for updates after the 100th epoch, where the learning rate $lr_{\text{epoch}} = lr_0 \times \left(1 - \frac{\max(\text{epoch}, 100) - 100}{50} \right)$.

D. Training and Evaluation Settings

To draw a comprehensive performance analysis, we set up three different evaluation schemes and their corresponding training strategies. In the test phase, to predict and reconstruct depth maps (denoted as \mathcal{T}), we used three different inputs in the three settings respectively, which are the raw depth maps (\mathcal{R}), randomly-sampled sparse depth maps (\mathcal{R}^*) from the raw depth maps, and randomly-sampled sparse depth maps (\mathcal{T}^*)

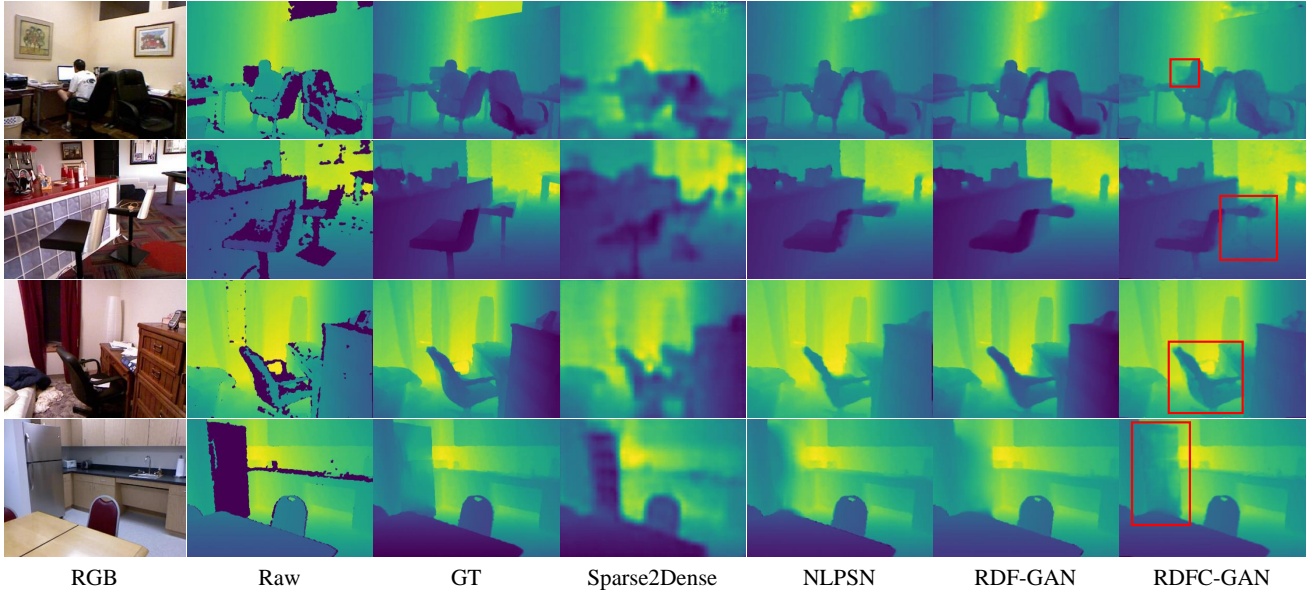


Fig. 8. Depth completion comparisons on NYU-Depth V2 with $\mathcal{R} \Rightarrow \mathcal{T}$.

from the reconstructed depth maps. The three settings are as the following specified:

- *Setting A* ($\mathcal{R} \Rightarrow \mathcal{T}$): To be the most in line with the real scenario of indoor depth completion, we input a raw depth map without downsampling during testing. At the training time, we used the pseudo depth maps (\mathcal{R}^{ps}) as the input and supervised with the raw depth image, to train NLSPN [14], GraphCSPN [38], RDF-GAN [1], and the proposed RDFC-GAN. Meanwhile, we compared with several baselines [12], [35]–[37] that were trained in the synthetic semi-dense sensor data [37].
- *Setting B* ($\mathcal{R}^* \Rightarrow \mathcal{T}$): Following a few previous works [9], [10], [14], we used a sparse depth map with 500 randomly sampled depth pixels of the *raw* depth image as the input during testing. In the training stage, the input was the same as that for testing, but the ground truth was the raw depth due to the unavailability of completed depth maps.
- *Setting C* ($\mathcal{T}^* \Rightarrow \mathcal{T}$): For comparing more existing methods [9]–[11], [13], [14], [19], [33] that focus on depth completion in sparse scenes, we used a sparse depth map with 500 randomly sampled depth pixels of the *reconstructed* depth map as the input during testing. The training input and output ground truth were the same as those of *Setting B*. As illustrated in Fig. 2, the downsampled input in this setting reveals ground truth depth values that are unavailable in practice.

We used all three settings in the main experiments on NYU-Depth V2. While *Setting A* ($\mathcal{R} \Rightarrow \mathcal{T}$) is the most plausible for indoor depth completion, we included the other two settings for comprehensive comparisons and demonstrated the generality of our methods. We used *Setting A* in all other experiments.

TABLE I
QUANTITATIVE RESULTS ON THE NYU-DEPTH V2 DATASET.
SPARES2DENSE AND DGCG IN $\mathcal{T}^* \Rightarrow \mathcal{T}$ USED 200 SAMPLED PIXELS
WHILE OTHERS USED 500 PIXELS.

Setting	Method	RMSE ↓	Rel ↓	$\delta_{1.25} \uparrow$	$\delta_{1.25^2} \uparrow$	$\delta_{1.25^3} \uparrow$
<i>Setting A</i> $\mathcal{R} \Rightarrow \mathcal{T}$	DC-BCS [12]	0.271	0.016	98.1	99.1	99.4
	RGB-GU [35]	0.260	0.017	97.9	99.3	99.7
	MS-CHN [36]	0.190	0.018	98.8	99.7	99.9
	DM-LRN [37]	0.205	0.014	98.8	99.6	99.9
	NLSPN [14]	0.153	0.015	98.6	99.6	99.9
	GraphCSPN [38]	<u>0.133</u>	0.015	98.7	99.7	99.9
	RDF-GAN [1]	0.139	<u>0.013</u>	98.7	99.6	99.9
RDFC-GAN	0.120	0.012	98.8	99.7	99.9	
<i>Setting B</i> $\mathcal{R}^* \Rightarrow \mathcal{T}$	Sparse2Dense [10]	0.335	0.060	94.2	97.1	98.8
	CSPN [9]	0.500	0.139	85.7	92.9	96.3
	NLSPN [14]	0.348	0.043	93.0	96.7	98.5
	GraphCSPN [38]	0.299	0.082	94.6	98.7	99.6
	GAENet [34]	<u>0.260</u>	0.067	94.7	98.9	99.7
	RDF-GAN [1]	0.309	0.053	93.6	97.6	99.0
RDFC-GAN	0.242	<u>0.047</u>	96.1	99.1	99.7	
<i>Setting C</i> $\mathcal{T}^* \Rightarrow \mathcal{T}$	Sparse2Dense [10]	0.230	0.044	97.1	99.4	99.8
	CSPN [9]	0.117	0.016	99.2	99.9	100.0
	3coeff [33]	0.131	0.013	97.9	99.3	99.8
	DGCG [13]	0.225	0.046	97.2		
	DeepLidar [11]	0.115	0.022	99.3	99.9	100.0
	NLSPN [14]	<u>0.092</u>	0.012	99.6	99.9	100.0
	PRR [19]	0.104	0.014	99.4	99.9	100.0
	GraphCSPN [38]	0.090	0.012	99.6	99.9	100.0
	GAENet [34]	0.114	0.018	99.3	99.9	100.0
RDF-GAN [1]	0.103	0.016	99.4	99.9	100.0	
RDFC-GAN	0.094	0.012	99.6	99.9	100.0	

E. Comparisons with State-of-the-Art Methods

1) *NYU-Depth V2*: The performance comparison on depth maps of our method and the other state-of-the-art methods on NYU-Depth V2 are shown in Tab. I. Given the results, we concluded the following:

- In the most realistic setting of $\mathcal{R} \Rightarrow \mathcal{T}$, compared to all the baselines, RDFC-GAN had significantly superior performance and obtained moderate improvement over the previous RDF-GAN, leading to remarkably *RMSE* of 0.120 and *Rel* of 0.012.
- We selected a few representative scenes and visualized

the completion results from different methods with the setting of $\mathcal{R} \Rightarrow \mathcal{T}$ in Fig. 8. RDFC-GAN produced more accurate and textured depth predictions in the missing depth regions. For example, the results within the red boxes clearly depicted the contour and depth information of subtle objects (laptops and chairs) and large missing ones (doors).

- In the setting of $\mathcal{R}^* \Rightarrow \mathcal{T}$, RDFC-GAN outperformed the baselines with big margins on $RMSE$, and achieved the best on all δ_{th} metrics and the second best on Rel . Also, RDFC-GAN improved RDF-GAN substantially by a 22% relative improvement on $RMSE$, indicating the efficacy of the newly proposed CycleGAN and Manhattan constraint components.
- We observed a similar trend in the setting of $\mathcal{T}^* \Rightarrow \mathcal{T}$ that RDFC-GAN obtained the best on four of all five metrics. In terms of $RMSE$, RDFC-GAN without any iteration processing was only lower than NLSPN [11] and GraphCSPN [38] (but 1.2 \times and 1.5 \times faster in inference than them, respectively). The results are commendable because RDFC-GAN is not designed for the sparse setting.

TABLE II
QUANTITATIVE RESULTS ON SUN RGB-D IN Setting A ($\mathcal{R} \Rightarrow \mathcal{T}$).

Method	$RMSE \downarrow$	$Rel \downarrow$	$\delta_{1.25} \uparrow$	$\delta_{1.25^2} \uparrow$	$\delta_{1.25^3} \uparrow$
Sparse2Dense [10]	0.329	0.074	93.9	97.0	98.1
CSPN [9]	0.295	0.137	95.6	97.5	98.4
DeepLidar [11]	0.279	0.061	96.9	98.0	98.4
NLSPN [14]	0.267	0.063	97.3	98.1	98.5
RDF-GAN [1]	0.255	0.059	96.9	98.4	99.0
RDFC-GAN	0.214	0.040	97.0	99.1	99.8

2) *SUN RGB-D*: The results on SUN RGB-D in Setting A are shown in Tab. II. We observed the following:

- The depth completion task on SUN RGB-D is much more difficult than that on NYU-Depth V2. This may be due to the fact that SUN RGB-D encompasses a greater variety of scenes is sourced from various sensors. Nevertheless, our methods (RDF-GAN and RDFC-GAN) achieved the best performance in most metrics. Particularly, RDFC-GAN outperformed the best baselines by a large margin (e.g., 0.214 v.s. 0.267 on $RMSE$ and 0.040 v.s. 0.061 on Rel).
- As the threshold value of δ_{th} increased, the performance gap between RDFC-GAN and the best baseline enlarged (from -0.3 of $\delta_{1.25}$ to $+1.2$ of $\delta_{1.25^3}$). The results indicate that baselines failed to complete depth in some regions even the tolerance threshold went larger, while RDFC-GAN was more robust to local outliers.
- From the visualization results in Fig. 1, RDFC-GAN complemented the missing depth with detailed texture information for all different sensors, showing its great generality.

3) *Comparisons on Point Clouds*: In order to examine local accuracies and provide comprehensive comparisons, we selected a few representative baselines, converted their output depth maps on NYU-Depth V2 to point clouds, and measured performance with the point clouds. Based on the quantitative results in Tab. III and the visualization results in Fig. 9, we can draw the following conclusions:

TABLE III
QUANTITATIVE COMPARISONS IN POINT CLOUDS ON NYU-DEPTH V2.
UNIT OF CD : 1×10^{-4} METER.

Method	Setting A $\mathcal{R} \Rightarrow \mathcal{T}$		Setting B $\mathcal{R}^* \Rightarrow \mathcal{T}$		Setting C $\mathcal{T}^* \Rightarrow \mathcal{T}$	
	CD	F_1	CD	F_1	CD	F_1
Sparse2Dense [10]	526.26	0.73	531.59	0.69	808.55	0.58
CSPN [9]	42.35	0.86	334.51	0.82	174.33	0.88
NLSPN [14]	35.83	0.88	342.99	0.83	92.01	0.89
GraphCSPN [38]	52.28	0.94	296.88	0.86	89.40	0.90
GAENet [34]	710.36	0.89	<u>267.07</u>	<u>0.86</u>	47.39	0.95
RDF-GAN [1]	79.66	0.90	284.10	<u>0.86</u>	90.03	0.93
RDFC-GAN	33.15	0.95	249.05	0.87	<u>79.74</u>	<u>0.94</u>

- RDFC-GAN obtained the lowest Chamfer distance values and the highest averaged F1 scores in the first two settings and the second best in the other setting, indicating the superior performance in various experimental settings, especially the addressed indoor scenario.
- The visualization clearly demonstrated that RDFC-GAN completed depth maps of the missing regions stable and reasonable, while other methods made distorted or even incomplete estimations. The results highlighted the effectiveness of our proposed method in achieving more accurate completion results.

F. Ablation Studies

We conducted ablation studies on NYU-Depth V2 with the setting of $\mathcal{R} \Rightarrow \mathcal{T}$ that best reflects indoor scenarios.

TABLE IV
ABLATION STUDY RESULTS FOR THE MANHATTAN NORMAL MODULE.
‘PT’ REFERS TO PRE-TRAINING ON SCANNET. ‘FT’ REFERS TO PRE-TRAINING ON SCANNET AND FINE-TUNING ON NYU-DEPTH V2.

Case #	MCN Structures	$RMSE \downarrow$	$Rel \downarrow$	$\delta_{1.25} \uparrow$
A-1	Local Guidance [1]	0.146	0.021	98.7
A-2	Normal Generator (PT)	0.147	0.020	98.5
A-3	Normal Generator (FT)	0.132	0.020	98.8
A-4	Manhattan Normal Module	0.120	0.012	99.9

1) *The MCN Branch*: We evaluated the proposed MCN structure with the best alternative (i.e., the Local Guidance module) from our earlier model RDF-GAN [1] with the performance comparison shown in Tab. IV. With only the pretrained normal generator (Case A-2), the model performed comparably with the local guidance (Case A-1), which may be due to their similar network structure (U-Net). The fine-tuning step (Case A-3) enhanced the capacity of the normal generator with the $RMSE$ boosted from 0.147 to 0.132. Using the segmentation network and the corresponding losses (Case A-4) further improved the performance. Notably, the improvements of Case A-4 are more distinct in terms of Rel and δ , indicating that utilizing Manhattan assumptions could better fix invalid and unreasonable depth outliers.

2) *The RDFC-GAN Branch*: Tab. V shows the ablation study results for the GAN branch. The model without GAN (Case B-1) degenerated to a dual encoder-decoder structure. In that case, the completed depth maps were shaped towards

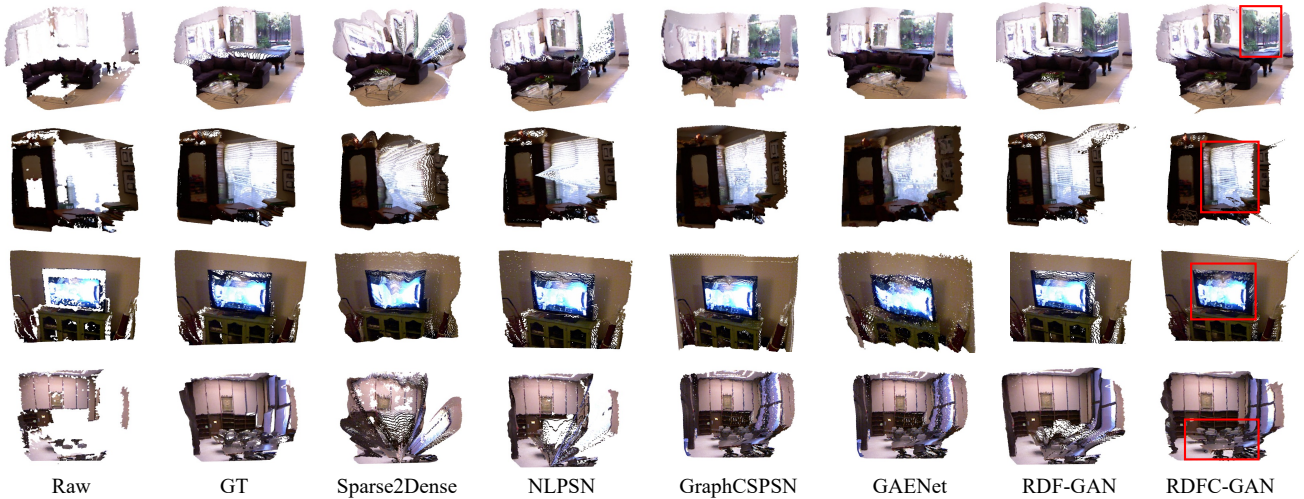


Fig. 9. Depth completion comparisons by point cloud visualizations on NYU-Depth V2 with $\mathcal{R} \Rightarrow \mathcal{T}$.

TABLE V
ABLATION STUDY RESULTS FOR THE CYCLEGAN. FOR CASES B-1 AND B-2, AN L_1 LOSS ON THE FUSION DEPTH MAP IS ADDED [1].

Case #	GAN Structures	$RMSE \downarrow$	$Rel \downarrow$	$\delta_{1.25} \uparrow$
B-1	No GAN	0.176	0.031	98.2
B-2	GAN	0.129	0.017	99.2
B-3	CycleGAN	0.120	0.012	99.9

a blurry one and the results were poor. Adding the GAN structure (Case B-2) substantially improved the performance, and using the CycleGAN [30] structure (Case B-3) led to further improvement (from 0.129 to 0.120 in terms of $RMSE$).

TABLE VI
ABLATION STUDY RESULTS FOR THE W-ADAİN MODULE.

Case #	Fusion Modules	$RMSE \downarrow$	$Rel \downarrow$	$\delta_{1.25} \uparrow$
C-1	IN [84]	0.126	0.016	99.0
C-2	AdaIN [27]	0.133	0.025	98.8
C-3	W-AdaIN	0.120	0.012	99.9

3) *The W-AdaIN Module*: As shown in Tab. VI, for the multi-stage fusion modules, W-AdaIN (Case C-1) outperformed the alternatives, i.e., IN [84] (Case C-2) and AdaIN [27] (Case C-3), by a clear margin. We also observed similar trend as in RDF-GAN [1] that AdaIN was slightly inferior to the original IN, indicating that directly applying the adaptive method may not for depth completion and our attention-based W-AdaIN is essential.

4) *The Two-Branch Structure*: In Fig. 10, we provide visualizations of three depth map completion outputs: d_1 from the MCN branch, d_f from the RDFC-GAN branch, and the final output d_{pred} . The MCN branch generated a precise depth map, albeit lacking distinct contours. The RDFC-GAN branch generated a depth map with more detailed textures while introducing a few noises and outliers. Significantly, with the help of the confidence fusion head, the complete RDFC-GAN

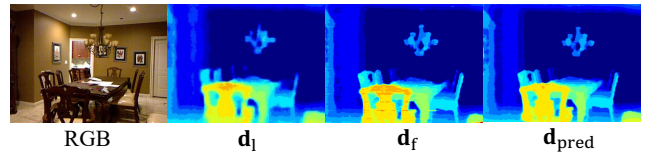


Fig. 10. Depth result visualizations of the MCN branch (d_1), the RDFC-GAN branch (d_f), and the entire model (d_{pred}).

model produced a final completion that is both precise and robust, taking advantage of both two branches.

TABLE VII
COMPARISONS OF 3D OBJECT DETECTION RESULTS WITH THE COMPLETED DEPTH MAP ON SUN RGB-D. THE LAST COLUMN IS THE DEPTH COMPLETION PERFORMANCE.

Method	$mAP@25 \uparrow$	$mAP@50 \uparrow$	$RMSE \downarrow$
VoteNet [85]	59.07	35.77	–
DeepLidar [11] + VoteNet [85]	59.73	35.49	0.279
NLSPN [14] + VoteNet [85]	47.43	26.10	0.267
RDF-GAN [1] + VoteNet [85]	60.64	37.28	0.255
RDFC-GAN + VoteNet [85]	61.02	37.47	0.214
H3DNet [86]	60.11	39.04	–
DeepLidar [11] + H3DNet [86]	60.35	39.16	0.279
NLSPN [14] + H3DNet [86]	27.10	9.77	0.267
RDF-GAN [1] + H3DNet [86]	<u>61.03</u>	<u>39.71</u>	<u>0.255</u>
RDFC-GAN + H3DNet [86]	61.75	40.63	0.214

G. Object Detection on the Completed Depth Map

We conducted extended experiments using completed depth maps as the input for 3D object detection on SUN RGB-D to evaluate the quality of our depth completions. Two SOTA models, VoteNet [85] and H3DNet [86], were used as the detectors. Tab. VII shows that both detectors obtained a significant improvement with our completed depth map. Meanwhile, DeepLidar [11] improved little in terms of the detection metrics; NLSPN [14] produced too much noise in the completion and even impaired the detection performance.

V. CONCLUSION

In this work, we propose a novel two-branch end-to-end network, RDFC-GAN, for indoor depth completion. We design a RGB-depth fusion CycleGAN model to produce the fine-grained textural depth map and restraint it by a Manhattan-constraint network. In addition, we propose a novel and effective sampling method to produce pseudo depth maps for training indoor depth completion models. Extensive experiments have demonstrated that our proposed solution achieves state-of-the-art on the NYU-Depth V2 and SUN RGB-D datasets.

ACKNOWLEDGMENTS

This work was supported in part by the BUPT Excellent Ph.D. Students Foundation under Grant CX2022224, the National Key R&D Program of China under Grant 2022YFF0904304, the Funds for International Cooperation and Exchange of NSFC under Grant 61720106007, the Fundamental Research Funds for the Central Universities under Grant 2019XD-A03-3, the 111 Project under Grant B18008, Shanghai Pujiang Program under Grant 21PJ1420300, and the Science and Technology Innovation Action Plan of Shanghai under Grant 22511105400.

REFERENCES

- [1] H. Wang, M. Wang, Z. Che, Z. Xu, X. Qiao, M. Qi, F. Feng, and J. Tang, "Rgb-depth fusion gan for indoor depth completion," in *Proceedings of the IEEE/CVF Conference on Computer Vision and Pattern Recognition*, 2022, pp. 6209–6218.
- [2] S. Song, S. P. Lichtenberg, and J. Xiao, "Sun rgb-d: A rgb-d scene understanding benchmark suite," in *Proceedings of the IEEE Conference on Computer Vision and Pattern Recognition (CVPR)*, 2015, pp. 567–576.
- [3] Y. Fu, Q. Yan, L. Yang, J. Liao, and C. Xiao, "Texture mapping for 3d reconstruction with rgb-d sensor," in *Proceedings of the IEEE Conference on Computer Vision and Pattern Recognition (CVPR)*, June 2018.
- [4] B. Li, J. P. Munoz, X. Rong, Q. Chen, J. Xiao, Y. Tian, A. Ardit, and M. Yousuf, "Vision-based mobile indoor assistive navigation aid for blind people," *IEEE Transactions on Mobile Computing (TMC)*, vol. 18, no. 3, pp. 702–714, 2019.
- [5] Y. Zhao and T. Guo, "Pointar: Efficient lighting estimation for mobile augmented reality," in *European Conference on Computer Vision (ECCV)*. Springer, 2020, pp. 678–693.
- [6] Microsoft, "Kinect for windows." [Online]. Available: <https://developer.microsoft.com/en-us/windows/kinect/>
- [7] L. Keselman, J. Iselin Woodfill, A. Grunnet-Jepsen, and A. Bhowmik, "Intel realsense stereoscopic depth cameras," in *Proceedings of the IEEE Conference on Computer Vision and Pattern Recognition (CVPR) Workshops*, July 2017.
- [8] ASUS, "Asus xtion." [Online]. Available: www.asus.com/Multimedia/Xtion_PRO/
- [9] X. Cheng, P. Wang, and R. Yang, "Depth estimation via affinity learned with convolutional spatial propagation network," in *Proceedings of the European Conference on Computer Vision (ECCV)*, 2018, pp. 103–119.
- [10] F. Ma and S. Karaman, "Sparse-to-dense: Depth prediction from sparse depth samples and a single image," in *2018 IEEE international conference on robotics and automation (ICRA)*. IEEE, 2018, pp. 4796–4803.
- [11] J. Qiu, Z. Cui, Y. Zhang, X. Zhang, S. Liu, B. Zeng, and M. Pollefeys, "DeepLidar: Deep surface normal guided depth prediction for outdoor scene from sparse lidar data and single color image," in *Proceedings of the IEEE Conference on Computer Vision and Pattern Recognition (CVPR)*, 2019, pp. 3313–3322.
- [12] Y.-K. Huang, T.-H. Wu, Y.-C. Liu, and W. H. Hsu, "Indoor depth completion with boundary consistency and self-attention," in *Proceedings of the IEEE/CVF International Conference on Computer Vision (ICCV) Workshops*, Oct 2019.
- [13] B.-U. Lee, H.-G. Jeon, S. Im, and I. S. Kweon, "Depth completion with deep geometry and context guidance," in *2019 International Conference on Robotics and Automation (ICRA)*. IEEE, 2019, pp. 3281–3287.
- [14] J. Park, K. Joo, Z. Hu, C.-K. Liu, and I. So Kweon, "Non-local spatial propagation network for depth completion," in *European Conference on Computer Vision (ECCV)*. Springer, 2020, pp. 120–136.
- [15] A. Saxena, S. H. Chung, and A. Y. Ng, "Learning depth from single monocular images," in *NIPS*, 2005.
- [16] M. Liu, M. Salzmann, and X. He, "Discrete-continuous depth estimation from a single image," in *Proceedings of the IEEE Conference on Computer Vision and Pattern Recognition (CVPR)*, 2014, pp. 716–723.
- [17] Q. Yang, "Stereo matching using tree filtering," *IEEE Transactions on Pattern Analysis and Machine Intelligence (PAMI)*, vol. 37, no. 4, pp. 834–846, 2014.
- [18] S. Liu, S. De Mello, J. Gu, G. Zhong, M.-H. Yang, and J. Kautz, "Learning affinity via spatial propagation networks," in *NIPS*, 2017.
- [19] B.-U. Lee, K. Lee, and I. S. Kweon, "Depth completion using plane-residual representation," in *Proceedings of the IEEE/CVF Conference on Computer Vision and Pattern Recognition (CVPR)*, June 2021, pp. 13 916–13 925.
- [20] Y. Lin, T. Cheng, Q. Zhong, W. Zhou, and H. Yang, "Dynamic spatial propagation network for depth completion," in *Proceedings of the AAAI Conference on Artificial Intelligence*, vol. 36, no. 2, 2022, pp. 1638–1646.
- [21] J. Coughlan and A. L. Yuille, "The manhattan world assumption: Regularities in scene statistics which enable bayesian inference," *Advances in Neural Information Processing Systems*, vol. 13, 2000.
- [22] R. Yunus, Y. Li, and F. Tombari, "Manhattanslam: Robust planar tracking and mapping leveraging mixture of manhattan frames," in *2021 IEEE International Conference on Robotics and Automation (ICRA)*. IEEE, 2021, pp. 6687–6693.
- [23] B. Li, Y. Huang, Z. Liu, D. Zou, and W. Yu, "Structdepth: Leveraging the structural regularities for self-supervised indoor depth estimation," in *Proceedings of the IEEE/CVF International Conference on Computer Vision (ICCV)*, October 2021, pp. 12 663–12 673.
- [24] H. Guo, S. Peng, H. Lin, Q. Wang, G. Zhang, H. Bao, and X. Zhou, "Neural 3d scene reconstruction with the manhattan-world assumption," in *Proceedings of the IEEE/CVF Conference on Computer Vision and Pattern Recognition*, 2022, pp. 5511–5520.
- [25] M. Mirza and S. Osindero, "Conditional generative adversarial nets," *arXiv preprint arXiv:1411.1784*, 2014.
- [26] T. Kim, M. Cha, H. Kim, J. K. Lee, and J. Kim, "Learning to discover cross-domain relations with generative adversarial networks," in *International conference on machine learning*. PMLR, 2017, pp. 1857–1865.
- [27] T. Karras, S. Laine, and T. Aila, "A style-based generator architecture for generative adversarial networks," in *Proceedings of the IEEE/CVF Conference on Computer Vision and Pattern Recognition (CVPR)*, June 2019.
- [28] J. Ma, W. Yu, P. Liang, C. Li, and J. Jiang, "Fusiongan: A generative adversarial network for infrared and visible image fusion," *Information Fusion*, vol. 48, pp. 11–26, 2019.
- [29] P. Isola, J.-Y. Zhu, T. Zhou, and A. A. Efros, "Image-to-image translation with conditional adversarial networks," in *Proceedings of the IEEE Conference on Computer Vision and Pattern Recognition (CVPR)*, July 2017.
- [30] J.-Y. Zhu, T. Park, P. Isola, and A. A. Efros, "Unpaired image-to-image translation using cycle-consistent adversarial networks," in *Computer Vision (ICCV), 2017 IEEE International Conference on*, 2017.
- [31] C. Zhang, Y. Tang, C. Zhao, Q. Sun, Z. Ye, and J. Kurths, "Multitask gans for semantic segmentation and depth completion with cycle consistency," *IEEE Transactions on Neural Networks and Learning Systems*, vol. 32, no. 12, pp. 5404–5415, 2021.
- [32] Z. Yan, K. Wang, X. Li, Z. Zhang, J. Li, and J. Yang, "Rignet: Repetitive image guided network for depth completion," in *Computer Vision–ECCV 2022: 17th European Conference, Tel Aviv, Israel, October 23–27, 2022, Proceedings, Part XXVII*. Springer, 2022, pp. 214–230.
- [33] S. Imran, Y. Long, X. Liu, and D. Morris, "Depth coefficients for depth completion," in *Proceedings of the IEEE/CVF Conference on Computer Vision and Pattern Recognition (CVPR)*, June 2019.
- [34] H. Chen, H. Yang, Y. Zhang *et al.*, "Depth completion using geometry-aware embedding," in *2022 International Conference on Robotics and Automation (ICRA)*. IEEE, 2022, pp. 8680–8686.
- [35] W. Van Gansbeke, D. Neven, B. De Brabandere, and L. Van Gool, "Sparse and noisy lidar completion with rgb guidance and uncertainty," in *2019 16th international conference on machine vision applications (MVA)*. IEEE, 2019, pp. 1–6.

- [36] A. Li, Z. Yuan, Y. Ling, W. Chi, s. zhang, and C. Zhang, "A multi-scale guided cascade hourglass network for depth completion," in *Proceedings of the IEEE/CVF Winter Conference on Applications of Computer Vision (WACV)*, March 2020.
- [37] D. Senushkin, M. Romanov, I. Belikov, N. Patakin, and A. Konushin, "Decoder modulation for indoor depth completion," in *IEEE/RSJ International Conference on Intelligent Robots and Systems, IROS 2021, Prague, Czech Republic, September 27 - Oct. 1, 2021*. IEEE, 2021, pp. 2181–2188.
- [38] X. Liu, X. Shao, B. Wang, Y. Li, and S. Wang, "Graphcspn: Geometry-aware depth completion via dynamic gcns," in *Computer Vision—ECCV 2022: 17th European Conference, Tel Aviv, Israel, October 23–27, 2022, Proceedings, Part XXXIII*. Springer, 2022, pp. 90–107.
- [39] X. Chen, K.-Y. Lin, J. Wang, W. Wu, C. Qian, H. Li, and G. Zeng, "Bi-directional cross-modality feature propagation with separation-and-aggregation gate for rgb-d semantic segmentation," in *Computer Vision—ECCV 2020: 16th European Conference, Glasgow, UK, August 23–28, 2020, Proceedings, Part XI*. Springer, 2020, pp. 561–577.
- [40] J. Cao, H. Leng, D. Lischinski, D. Cohen-Or, C. Tu, and Y. Li, "Shapeconv: Shape-aware convolutional layer for indoor rgb-d semantic segmentation," in *Proceedings of the IEEE/CVF international conference on computer vision*, 2021, pp. 7088–7097.
- [41] H. Zhou, L. Qi, H. Huang, X. Yang, Z. Wan, and X. Wen, "Canet: Co-attention network for rgb-d semantic segmentation," *Pattern Recognition*, vol. 124, p. 108468, 2022.
- [42] A. Bozic, M. Zollhofer, C. Theobalt, and M. Nießner, "Deepdeform: Learning non-rigid rgb-d reconstruction with semi-supervised data," in *Proceedings of the IEEE/CVF Conference on Computer Vision and Pattern Recognition*, 2020, pp. 7002–7012.
- [43] S.-C. Wu, J. Wald, K. Tateno, N. Navab, and F. Tombari, "Scenegrph-fusion: Incremental 3d scene graph prediction from rgb-d sequences," in *Proceedings of the IEEE/CVF Conference on Computer Vision and Pattern Recognition*, 2021, pp. 7515–7525.
- [44] D. Azinović, R. Martin-Brualla, D. B. Goldman, M. Nießner, and J. Thies, "Neural rgb-d surface reconstruction," in *Proceedings of the IEEE/CVF Conference on Computer Vision and Pattern Recognition*, 2022, pp. 6290–6301.
- [45] P. Karkus, S. Cai, and D. Hsu, "Differentiable slam-net: Learning particle slam for visual navigation," in *Proceedings of the IEEE/CVF Conference on Computer Vision and Pattern Recognition*, 2021, pp. 2815–2825.
- [46] Z. Teed and J. Deng, "Droid-slam: Deep visual slam for monocular, stereo, and rgb-d cameras," *Advances in neural information processing systems*, vol. 34, pp. 16 558–16 569, 2021.
- [47] "Visual slam for robot navigation in healthcare facility," *Pattern Recognition*, vol. 113, p. 107822, 2021.
- [48] M. Maire, T. Narihira, and S. X. Yu, "Affinity cnn: Learning pixel-centric pairwise relations for figure/ground embedding," in *Proceedings of the IEEE Conference on Computer Vision and Pattern Recognition (CVPR)*, 2016, pp. 174–182.
- [49] Y. Cheng, R. Cai, Z. Li, X. Zhao, and K. Huang, "Locality-sensitive deconvolution networks with gated fusion for rgb-d indoor semantic segmentation," in *Proceedings of the IEEE Conference on Computer Vision and Pattern Recognition (CVPR)*, 2017, pp. 3029–3037.
- [50] S.-J. Park, K.-S. Hong, and S. Lee, "Rdfnet: Rgb-d multi-level residual feature fusion for indoor semantic segmentation," in *Proceedings of the IEEE International Conference on Computer Vision (ICCV)*, 2017, pp. 4980–4989.
- [51] D. Du, L. Wang, H. Wang, K. Zhao, and G. Wu, "Translate-to-recognize networks for rgb-d scene recognition," in *Proceedings of the IEEE/CVF Conference on Computer Vision and Pattern Recognition (CVPR)*, June 2019.
- [52] C.-T. Lin, S.-W. Huang, Y.-Y. Wu, and S.-H. Lai, "Gan-based day-to-night image style transfer for nighttime vehicle detection," *IEEE Transactions on Intelligent Transportation Systems*, vol. 22, no. 2, pp. 951–963, 2020.
- [53] H. Emami, M. M. Aliabadi, M. Dong, and R. B. Chinnam, "Spa-gan: Spatial attention gan for image-to-image translation," *IEEE Transactions on Multimedia*, vol. 23, pp. 391–401, 2020.
- [54] R. Li, "Image style transfer with generative adversarial networks," in *Proceedings of the 29th ACM International Conference on Multimedia*, 2021, pp. 2950–2954.
- [55] H. Liu, Z. Wan, W. Huang, Y. Song, X. Han, and J. Liao, "Pd-gan: Probabilistic diverse gan for image inpainting," in *Proceedings of the IEEE/CVF Conference on Computer Vision and Pattern Recognition*, 2021, pp. 9371–9381.
- [56] M. Afifi, M. A. Brubaker, and M. S. Brown, "Histogan: Controlling colors of gan-generated and real images via color histograms," in *Proceedings of the IEEE/CVF conference on computer vision and pattern recognition*, 2021, pp. 7941–7950.
- [57] F. Zhan, H. Zhu, and S. Lu, "Spatial fusion gan for image synthesis," in *Proceedings of the IEEE/CVF conference on computer vision and pattern recognition*, 2019, pp. 3653–3662.
- [58] E. R. Chan, M. Monteiro, P. Kellnhöfer, J. Wu, and G. Wetzstein, "pi-gan: Periodic implicit generative adversarial networks for 3d-aware image synthesis," in *Proceedings of the IEEE/CVF conference on computer vision and pattern recognition*, 2021, pp. 5799–5809.
- [59] J.-Y. Zhu, T. Park, P. Isola, and A. A. Efros, "Unpaired image-to-image translation using cycle-consistent adversarial networks," in *Proceedings of the IEEE international conference on computer vision*, 2017, pp. 2223–2232.
- [60] C. Zou, A. Colburn, Q. Shan, and D. Hoiem, "Layoutnet: Reconstructing the 3d room layout from a single rgb image," in *Proceedings of the IEEE conference on computer vision and pattern recognition*, 2018, pp. 2051–2059.
- [61] C. Lin, C. Li, and W. Wang, "Floorplan-jigsaw: Jointly estimating scene layout and aligning partial scans," in *Proceedings of the IEEE/CVF International Conference on Computer Vision*, 2019, pp. 5674–5683.
- [62] S.-T. Yang, F.-E. Wang, C.-H. Peng, P. Wonka, M. Sun, and H.-K. Chu, "Dula-net: A dual-projection network for estimating room layouts from a single rgb panorama," in *Proceedings of the IEEE/CVF Conference on Computer Vision and Pattern Recognition*, 2019, pp. 3363–3372.
- [63] G. Pintore, M. Agus, and E. Gobbetti, "Atlantnet: inferring the 3d indoor layout from a single 360° image beyond the manhattan world assumption," in *Computer Vision—ECCV 2020: 16th European Conference, Glasgow, UK, August 23–28, 2020, Proceedings, Part VIII*. Springer, 2020, pp. 432–448.
- [64] C. Zou, J.-W. Su, C.-H. Peng, A. Colburn, Q. Shan, P. Wonka, H.-K. Chu, and D. Hoiem, "Manhattan room layout reconstruction from a single 360° image: A comparative study of state-of-the-art methods," *International Journal of Computer Vision*, vol. 129, pp. 1410–1431, 2021.
- [65] Y. Zhang, S. Song, P. Tan, and J. Xiao, "Panocontext: A whole-room 3d context model for panoramic scene understanding," in *Computer Vision—ECCV 2014: 13th European Conference, Zurich, Switzerland, September 6–12, 2014, Proceedings, Part VI 13*. Springer, 2014, pp. 668–686.
- [66] Y. Furukawa, B. Curless, S. M. Seitz, and R. Szeliski, "Manhattan-world stereo," in *2009 IEEE Conference on Computer Vision and Pattern Recognition*. IEEE, 2009, pp. 1422–1429.
- [67] M. Li, P. Wonka, and L. Nan, "Manhattan-world urban reconstruction from point clouds," in *Computer Vision—ECCV 2016: 14th European Conference, Amsterdam, The Netherlands, October 11–14, 2016, Proceedings, Part IV 14*. Springer, 2016, pp. 54–69.
- [68] V. Patil, C. Sakaridis, A. Liniger, and L. Van Gool, "P3depth: Monocular depth estimation with a piecewise planarity prior," in *Proceedings of the IEEE/CVF Conference on Computer Vision and Pattern Recognition*, 2022, pp. 1610–1621.
- [69] J. Xu, X. Liu, Y. Bai, J. Jiang, K. Wang, X. Chen, and X. Ji, "Multi-camera collaborative depth prediction via consistent structure estimation," in *Proceedings of the 30th ACM International Conference on Multimedia*, 2022, pp. 2730–2738.
- [70] H. Zhao, J. Shi, X. Qi, X. Wang, and J. Jia, "Pyramid scene parsing network," in *Proceedings of the IEEE conference on computer vision and pattern recognition*, 2017, pp. 2881–2890.
- [71] G. Bae, I. Budvytis, and R. Cipolla, "Estimating and exploiting the aleatoric uncertainty in surface normal estimation," in *Proceedings of the IEEE/CVF International Conference on Computer Vision*, 2021, pp. 13 137–13 146.
- [72] K. He, X. Zhang, S. Ren, and J. Sun, "Deep residual learning for image recognition," in *Proceedings of the IEEE Conference on Computer Vision and Pattern Recognition (CVPR)*, June 2016.
- [73] J. Deng, W. Dong, R. Socher, L.-J. Li, K. Li, and L. Fei-Fei, "Imagenet: A large-scale hierarchical image database," in *Proceedings of the IEEE Conference on Computer Vision and Pattern Recognition (CVPR)*. Ieee, 2009, pp. 248–255.
- [74] I. Gulrajani, F. Ahmed, M. Arjovsky, V. Dumoulin, and A. C. Courville, "Improved training of wasserstein gans," in *Advances in Neural Information Processing Systems*, I. Guyon, U. V. Luxburg, S. Bengio, H. Wallach, R. Fergus, S. Vishwanathan, and R. Garnett, Eds., vol. 30. Curran Associates, Inc., 2017.
- [75] A. Vaswani, N. Shazeer, N. Parmar, J. Uszkoreit, L. Jones, A. N. Gomez, Ł. Kaiser, and I. Polosukhin, "Attention is all you need," in *NIPS*, 2017, pp. 5998–6008.

- [76] S.-Y. Kim, M. Kim, and Y.-S. Ho, "Depth image filter for mixed and noisy pixel removal in rgb-d camera systems," *IEEE Transactions on Consumer Electronics*, vol. 59, no. 3, pp. 681–689, 2013.
- [77] M. Arnold, A. Ghosh, S. Ameling, and G. Lacey, "Automatic segmentation and inpainting of specular highlights for endoscopic imaging," *EURASIP Journal on Image and Video Processing*, vol. 2010, pp. 1–12, 2010.
- [78] E.-T. Baek, H.-J. Yang, S.-H. Kim, G. Lee, and H. Jeong, "Distance error correction in time-of-flight cameras using asynchronous integration time," *Sensors*, vol. 20, no. 4, p. 1156, 2020.
- [79] P. F. Felzenszwalb and D. P. Huttenlocher, "Efficient graph-based image segmentation," *International journal of computer vision (IJCV)*, vol. 59, no. 2, pp. 167–181, 2004.
- [80] O. Ronneberger, P. Fischer, and T. Brox, "U-net: Convolutional networks for biomedical image segmentation," in *International Conference on Medical image computing and computer-assisted intervention*. Springer, 2015, pp. 234–241.
- [81] P. K. Nathan Silberman, Derek Hoiem and R. Fergus, "Indoor segmentation and support inference from rgb-d images," in *European Conference on Computer Vision (ECCV)*, 2012.
- [82] I. Loshchilov and F. Hutter, "Decoupled weight decay regularization," in *International Conference on Learning Representations*, 2019.
- [83] D. P. Kingma and J. Ba, "Adam: A method for stochastic optimization," 2015.
- [84] X. Huang and S. Belongie, "Arbitrary style transfer in real-time with adaptive instance normalization," in *Proceedings of the IEEE International Conference on Computer Vision (ICCV)*, Oct 2017.
- [85] C. R. Qi, O. Litany, K. He, and L. J. Guibas, "Deep hough voting for 3d object detection in point clouds," in *Proceedings of the IEEE International Conference on Computer Vision (ICCV)*, 2019, pp. 9277–9286.
- [86] Z. Zhang, B. Sun, H. Yang, and Q. Huang, "H3dnet: 3d object detection using hybrid geometric primitives," in *Proceedings of the European Conference on Computer Vision (ECCV)*. Springer, 2020, pp. 311–329.